ACS OMEGA

http://pubs.acs.org/journal/acsodf

Article

Highly Sensitive Dual-Band Terahertz Metamaterial Absorber for Biomedical Applications: Simulation and Experiment

Yadgar I. Abdulkarim, Olcay Altintas, Ayoub Sabir Karim, Halgurd N. Awl, Fahmi F. Muhammadsharif, Fatih Özkan Alkurt, Mehmet Bakir, Bhargav Appasani, Muharrem Karaaslan, and Jian Dong*

Cite This: *ACS Omega* 2022, 7, 38094−38104

Read Online

ACCESS | Metrics & More | Article Recommendations

ABSTRACT: In this paper, a terahertz (THz) metamaterial absorber (MTMA), incorporating surface Pythagorean tree fractal resonators, was designed and experimentally fabricated on the flexible substrate of polyethylene terephthalate. The design presented two peaks with strong absorption of more than 97% at 0.49 and 0.69 THz. The dual-band absorption peaks were seen to be shifted with the change in the refractive index of the surrounding medium, with a corresponding sensitivity of 0.0968 and 0.1182 THz/RIU. The spectral shift of the reflection resonance dip was utilized as an assessment index to evaluate the sensing performance of the new structure, and it was found to be 2.08 and 2.98 for the two resonance peaks, respectively. It was observed that the proposed structure acted as an epsilon negative material at the first resonance and as a mu negative material at the second resonance. Further investigations on the electric field, magnetic field, and surface current distributions were carried out to elaborate on the absorption characteristics at various resonance frequencies. The proposed sensor is a highly sensitive MTMA which can be used to investigate the interaction of matter with THz waves.

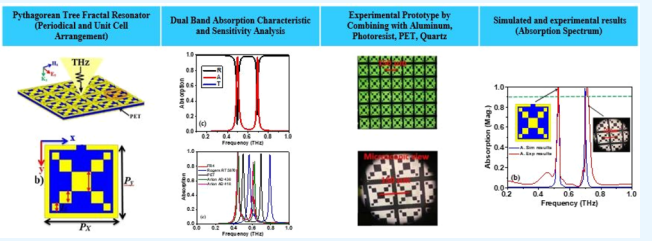

1. INTRODUCTION

In recent years, researchers have been interested in terahertz (THz) studies based on metamaterial (MTM) structures. MTMs are subwavelength structures that manipulate electromagnetic signals, exhibiting unnatural and exotic properties. They have effectively been used in various applications ranging from radio frequencies to optical microscopy. Researchers have used MTMs in cloaking,[1,2] optical lenses,[3,4] absorbers,[5−8] antennas,[9,10] polarization converters,[11,12] and sensors[13,14] with great success.

In the THz frequency range, studies were conducted to focus on continuous-wave THz imaging,[15,16] THz time-domain spectroscopy,[17−19] and THz near-field imaging.[20,21] The other topics of research in the terahertz regime are absorbers,[22−24] terahertz radiations,[25−27] waveguides,[28−30] wireless communications,[31,32] and sensors.[33−40] Research in the THz sensors focuses on discriminating nanoscaled biological or chemical samples as it is possible to measure their structural behavior in this frequency regime. These samples can be sensed and precisely measured by utilizing the extraordinary features of MTMs. Saadeldin et al. proposed an MTM absorber structure for THz biomedical sensing applications.[33] The sensor showed 99% of absorptivity at 2.249 THz with a *Q*-factor of 22.05. Also, it presented a sensitivity of 23.7 GHz/μm when it was used for the measurement of analyte thickness. Yang and Lin presented a tunable MTM-based THz sensor consisting of two concentric split-ring resonators.[34] The tuning range of the sensor was from 0.958 to 1.390 THz. Wang et al. analyzed a structure for sensing applications, having two identical square patches of unit cells.[35] The proposed structure offered an absorption of nearly 100% at 1.7780 and 2.4591 THz with respective quality factors of 6.9156 and 296.2771. Keshavarz and Vafapour numerically demonstrated an MTM-based THz biosensor structure, which was produced by an H-shaped graphene resonator on a semiconductor film.[36] The proposed sensor was able to detect three subtypes of avian influenza viruses with a great accuracy.

A highly sensitive MTM absorber-based THz sensor was suggested by Nickpay et al. for biomedical applications.[37] The proposed sensor structure consisted of graphene resonators, which can be used by adjusting the graphene layer with a DC bias voltage. The sensor had a nearly perfect absorption at 4 THz with an average *Q*-factor of 13.76. Furthermore, Yang et al. developed a THz MTM sensor to distinguish the normal

Received: September 22, 2022
Accepted: October 5, 2022
Published: October 14, 2022

glucose concentration from the abnormal one.[38] Asymmetric metals on a silicon dioxide substrate were used to design the sensor. Two transmission peak points were obtained at 0.26 and 0.4 THz. The sensor achieved a sensitivity of 1.22 and 0.52 THz per mol/L. Askari et al. suggested a refractive-index-based THz sensor for the detection of crystalline sugar molecules.[39] The structure exhibited narrow band characteristics at around 1.75 THz. The sensitivity of the proposed sensor was 7000 and 19.44 nm/RIU in practical applications. An all-metal MTM-based THz biosensor was investigated by Wang et al. for protein detection both theoretically and experimentally.[40] The experimental detection sensitivity was 72.81 GHz per ng/mm^2 with a detection limit of 0.035 mg/mL.

In the current research, a new THz metamaterial absorber (MTMA) is designed and fabricated by incorporating surface Pythagorean tree fractal resonators on the flexible polyethylene terephthalate (PET) substrate. The design showed two intense absorption peaks of more than 97% at 0.49 and 0.69 THz. The proposed sensor is specifically important to detect variations in the refractive index of the surrounding medium, thereby monitoring the interesting shift in the dual-band absorption peak. The novelty of the proposed absorber is the high Q-factor and refractive index sensing simultaneously (the trade-off between Q-factor and refraction sensing) through having a low profile design on the flexible PET substrate.

2. DESIGN OF THE UNIT CELL MODEL

The proposed MTM's unit cell is based on the Pythagorean tree fractal design, as shown in Figure 1. The proposed

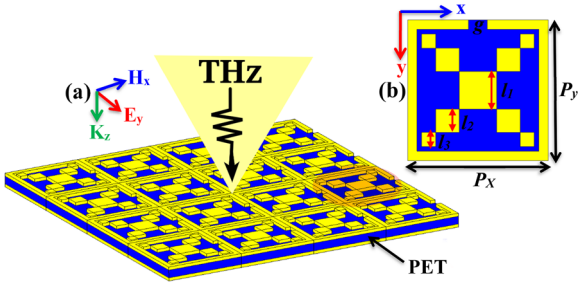

Figure 1. Images of a (a) 4 × 4 array proposed design and (b) unit cell of the MTM based on the Pythagorean tree fractal design, where the dimensions are denoted by $Px = Py = 150$ μm, $l_1 = 40$ μm, $l_2 = 25$ μm, $l_3 = 15$ μm, and $g = 20$ μm.

absorber was designed using a commercial full-wave finite integration technique (FIT) based on a high-frequency electromagnetic solver, CST microwave studio. Nowadays, CST makes it possible to use very difficult numerical calculations in the electromagnetic field through a number of software packages. Thus, the MTM characteristics can be determined using a number of numerical calculations. During the simulation phase, very complex and long calculations can be easily performed, and the behaviors of large-scale and very different shapes of MTM structures, under the selected frequency range and selected boundary conditions, can be demonstrated. Scientists have had the opportunity to test electromagnetic materials in the laboratory under various boundary conditions. In numerical analysis, various boundary conditions were used to analyze structures, such as PEC/PMC, PEC, free space, periodic arrays, and unit cells. In order to obtain the effective dimensions of the proposed structure and to simplify the simulation processes, a unit cell was assigned in the x-/y-directions, while an open add space was assigned to the z-direction. Figure 1a shows the schematic of a proposed 4 × 4 metamaterial array with a Pythagorean tree fractal shape, which is illuminated by a normally incident plane wave.

The model has a three-layered structure with aluminum metal on the top and bottom layers, while a dielectric spacer made of PET is used in the middle. The conductivity of aluminum is 3.56×10^7 S/m, and the dielectric spacer's thickness was $h = 10$ μm. The top and bottom aluminum layers were 0.2 μm thick. The bottom aluminum layer was sufficiently thick to prevent the transmission of electromagnetic waves. For a perfect absorption, the top metal layer has to be appropriately designed to match its impedance with that of the incident medium, which is the free space. With a high impedance match, the reflected electromagnetic energy is minimum, and hence a maximum power can penetrate and continue to propagate in the medium (PET). The required dimensions for metamaterial design unit cell are denoted by $Px = Py = 150$ μm, $l_1 = 40$ μm, $l_2 = 25$ μm, $l_3 = 15$ μm, and $g = 20$ μm (Figure 1b). The absorption coefficient (A) can be calculated from the following equation:

$$A = 1 - |S_{11}|^2 - |S_{12}|^2 \quad (1)$$

where S_{12} is the transmission coefficient (T), and s_{11} is the reflection coefficient (R). A strong absorption mechanism needs high electrical and/or magnetic losses to absorb traveling waves. These losses stem from the imaginary parts of the relative permittivity and/or permeability. In addition, the metallic layer at the bottom prevents the transmission of the waves, and hence, one can neglect the transmission (T). The structure was excited using a plane electromagnetic wave incident on the top plane, and then the absorption characteristics were obtained, as shown in Figure 2.

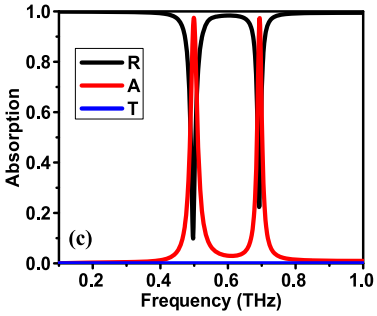

Figure 2. Absorption characteristics of the proposed unit cell.

It is observed from the figure that there are two absorption peaks at 0.49 and 0.69 THz, with a peak absorption of more than 97%. Designing the proposed unit cell model involves using a split-ring resonator and adding additional square patches until the desired absorption characteristics are achieved.

In this next step, we performed a comprehensive optimization process through variation of the resonator lengths, substrate thicknesses, and types of substrate materials, as well as from the modification of the substrate types and dielectric constants. These are significant differences between our work and the literature, where only fixed unit cells with different resonators have been investigated. Hence, the advantage of the proposed work is to employ a flexible PET substrate followed by using optimized Pythagorean tree fractal

https://doi.org/10.1021/acsomega.2c06118
ACS Omega 2022, 7, 38094−38104

resonators. With this design, it is possible to achieve a dual-band-based structure with high sensitivity. As such, the proposed MTM can be specifically important for the applications of biomedical sensing.

Based on the simulation results, the absorption spectra are integrated around the PET layers. When the substrate layer is incorporated with Pythagorean tree fractal resonators, the characteristic absorption peaks are merged together to expand the absorption bandwidth, thereby achieving three highly resonant peaks.

The absorption tunability of this design, which is born out of fractal arrangement of a central square patch, can be explained from the results shown in Figure 4. Without the surface fractals, the absorption is not significant in both of the bands. Also, the importance of this approach can be understood from the electric and magnetic field distributions shown in Figure 8. At 0.49 THz, the electric field is concentrated in the outer two square patches, whereas the magnetic field is concentrated in the central patch and its attached patch. Similarly, at 0.69 THz, the two outer patches contribute to the electric field distribution, along with the edge of the unit cell, and the magnetic field is concentrated at the second square patch on the top. Thus, the design with surface fractals plays an important role in the absorption.

Four different models have been created to observe the absorption characteristics up to 1 THz, and the unit cell with the best absorption characteristics is selected for further analyses. The four models have different metallic arrangements on the top, so their absorption spectra become different. The metallic portions on the top plane have to be properly designed to achieve the desired absorption characteristics. The four models include an outer split-ring resonator to provide magnetic resonance. At the center, a square patch is placed to increase the electrical resonance. Additional small square resonators are placed for different models to produce additional electric or magnetic resonances. These four-unit cell models are shown in Figure 3.

For all MTMAs, the thicknesses of the dielectric layer, the width of the metallic strip layers, and gaps are labeled as h = 10 μm, w = 10 μm, and g = 20 μm, respectively, where $t_1 = t_2$ = 0.2 are the thickness of the ground plate and resonator layer. $P_1 = l_1$ = 40 μm, $P_2 = l_2$ = 25 μm, and $P_3 = l_3$ = 15 μm are denoted for the length of the square resonator of model 1, model 2, and model 3, respectively. The absorption characteristics for the four models are shown in Figure 4.

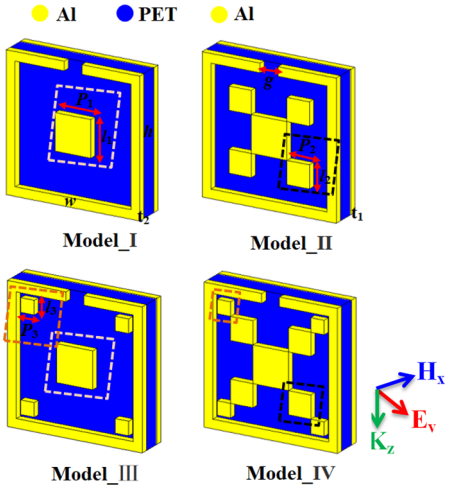

Figure 3. 3D schematic plot for the MA examples and the incident THz field polarizations.

The absorption characteristics show that model 2 and model 4 have two absorption peaks, while model 1 and model 3 have only one absorption peak at 0.7 THz. The similarity between the resonance frequencies of model 1 and model 3 shows that the added small metallic parts at the corners of the square patch do not affect the physical characteristic of the resonance. Model 2, with additional small square patches, offer dual-band absorption at 0.65 and 0.7 THz. The complete analysis requires electric and magnetic field distributions, which were not performed for these designs as their absorption is not significant compared to that of the proposed design. However, our analysis is based on the absorption mechanism in the famous split-ring resonator. Model 1 and model 3 have identical absorption characteristics, indicating an identical absorption mechanism. In model 1, there is a split-ring resonator, and it is well-known that magnetic resonance is the primary resonance mechanism in such structures.[41] In model 2, the resonance that occurs near 0.69 THz is significantly diminished, indicating an improper magnetic resonance. Model 4 has additional square patches resulting in enhanced resonance at 0.49 and 0.69 THz. The enhancement is due to the increased connected aluminum part on the top layer. Hence, it can be concluded that it is possible to create resonance and increase the absorption by a proper design of the top layer, and model 4 has the best absorption characteristics.

3. RESULTS AND DISCUSSION

The surface Pythagorean tree fractal resonator was chosen as the desired absorber structure, which is based on square shapes of resonators with different sizes and a square split-ring resonator to enhance the electrical and magnetic response of the structure. The choice of the design parameters is justified in terms of the substrate thickness (h), length of square resonators (l), and the substrate material.

3.1. Parameter Optimization. To investigate the effect of changing the substrate thickness on the absorption performance, the thickness (h) was increased from 0.6 to 14 μm, as illustrated in Figure 5a. The results showed that changing the thickness did not provide any significant changes in the second absorption peak. The first absorption peak was located at 0.49 THz, and both of the peaks showed a high absorption value at 10 μm of thickness.

Figure 5b shows the simulated results for varied lengths of the square resonators from 36 to 44 μm in steps of 0.2 μm. One can see from the curve that the length of the square resonator did not affect the second absorption peak, which remained constant at 0.69 THz with the same absorption value of 0.97. The decreased length (l) caused a slight shift in the frequency of the first peak to the higher frequency with the same absorption of 0.97. In the third case, the absorption performance was investigated by changing the substrate types, which are FR-4, Rogers RT5780, PET, Arlon AD 430, and Arlon AD 410. There are several materials reported in the literature and can be found on the market such as FR4 and Rogers. They are mostly used as a substrate layer in various applications. In this study, we tested FR4 and Rogers materials for dielectric variations and their effects. In some printed circuit board "PCB" processes, FR4 and Rogers 5870 are difficult to apply to the terahertz frequency band. We have

https://doi.org/10.1021/acsomega.2c06118
ACS Omega 2022, 7, 38094−38104

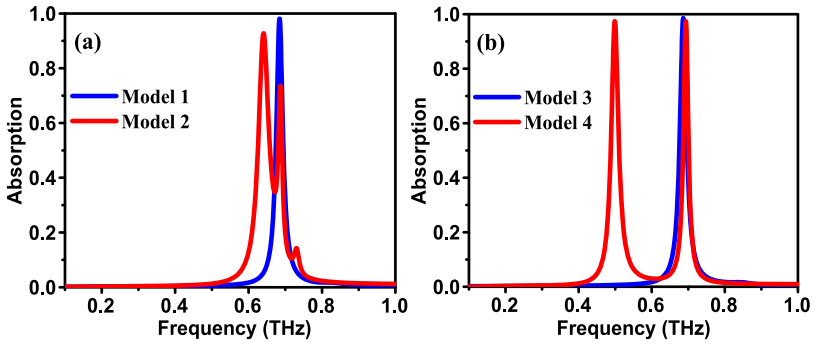

Figure 4. Absorption characteristics of the four unit cells: (a) model 1 and model 2 and (b) model 3 and model 4.

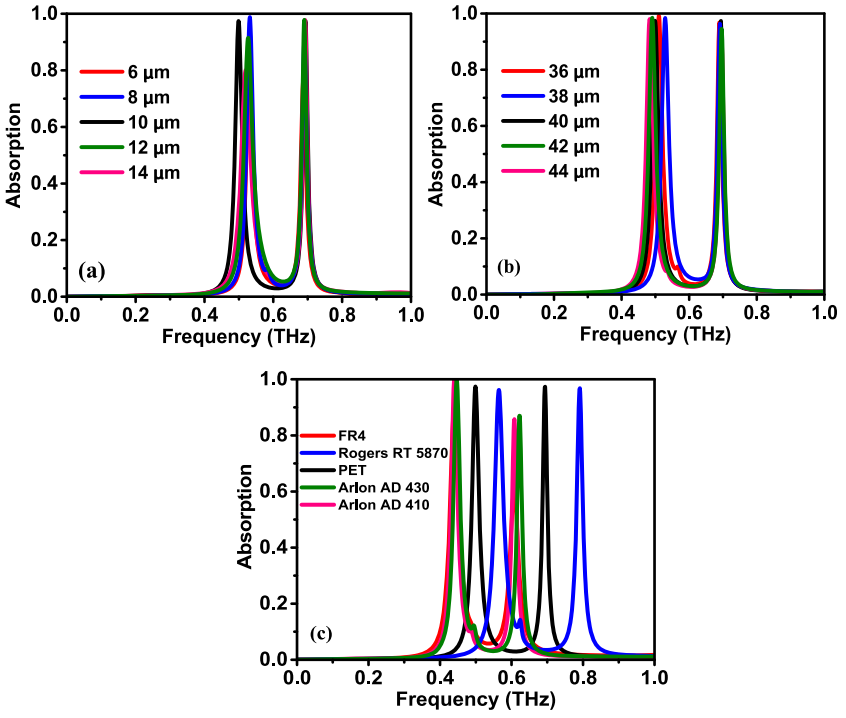

Figure 5. Absorption spectra of the proposed design under different (a) resonator lengths, (b) substrate thicknesses, and (c) types of the material substrates.

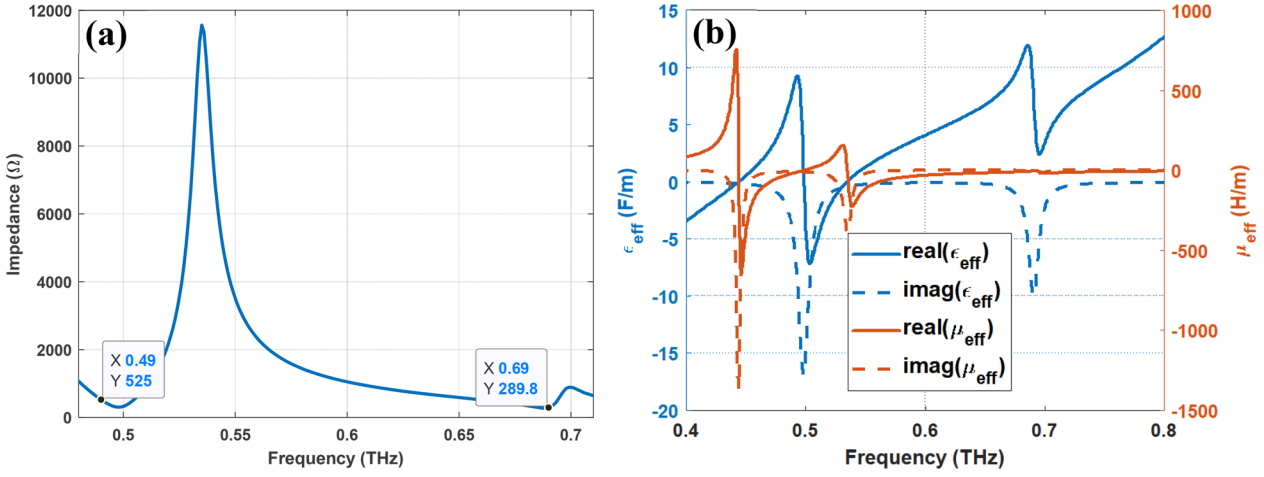

Figure 6. (a) Impedance plot and (b) effective permeability and permittivity plot.

used the PET dielectric layer as a substrate due to its ease of implementation in the lithographic technique for the terahertz frequency regions. In contrast to the substrate thickness and length of square resonators, the change in the substrate

https://doi.org/10.1021/acsomega.2c06118
ACS Omega 2022, 7, 38094−38104

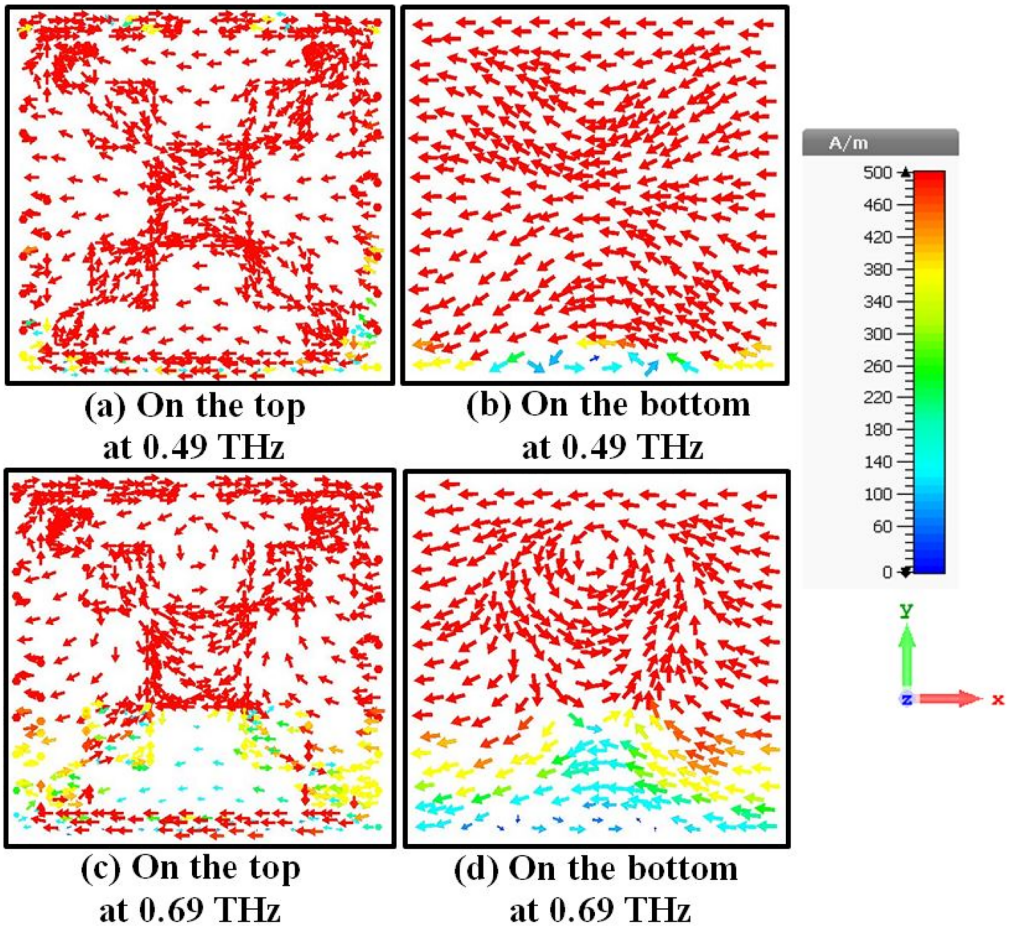

Figure 7. Surface current distribution of the proposed metamaterial design (a) at 0.49 THz on the top, (b) at 0.49 THz on the bottom, (c) at 0.69 THz on the top, and (d) at 0.69 THz on the bottom.

material strongly affects the achieved results. One can see from Figure 5c that both materials, Arlon AD 430 and Arlon AD 410, provide the same absorption value for the first peak at 0.43 and 0.44 THz, respectively, whereas for the second peak, Arlon AD 430 resulted in 0.85 absorption at 0.60 THz. On the contrary, Arlon AD 410 has a higher absorption of about 0.87 at the frequency of 0.62 THz. The other materials, FR4 and Rogers RT5870, offered two high absorption peaks with absorption values of more than 0.95 at different frequencies. The two peaks of PET material resonate at 0.49 and 0.69 THz, whereas the two peaks obtained with Rogers RT5780 material resonate at high frequencies of 0.59 and 0.79 THz.

3.2. Resonance Mechanism. The impedance (Z_{11}) plot is given in Figure 6a to explain the resonance phenomenon. Resonance occurs when the impedance matches with the free space impedance which is approximately 377 Ω. One can see from the impedance plot that the first peak at 0.49 THz has an impedance of 525 Ω, while the second peak at 0.69 THz has an impedance of 289.8 Ω. The effective permeability (ε_{eff}) and permittivity (μ_{eff}) are also obtained and are plotted in Figure 6b. For the first resonance at 0.49 THz, ε_{eff} is negative, and μ_{eff} is positive, indicating that the material is epsilon negative material (ENM) and the resonance is plasmonic in nature. The second resonance at 0.69 THz has ε_{eff} positive and μ_{eff} negative, implying that the material is mu negative material (MNM) and the resonance is magnetic. The magnetic resonance is necessary for the refractive index to be negative. A negative refractive index can be achieved when at least the permeability is negative. Thus, negative permeability (mu) indicates the presence of a magnetic resonance.[42] Thus, the design has a hybrid resonance mechanism, and the material behaves as an ENM during the first resonance and as an MNM during the second resonance mechanism.

To better understand the physical absorption mechanism of the proposed metamaterial absorbers, the surface current distribution of the top and bottom layers of the proposed design was studied. Parallel and antiparallel surface current distribution of the top layer is seen in Figure 7a, which reveals a magnetic dipole resonance mode. The surface currents on the metallic layers sometimes flow in opposite directions. This creates a magnetic flux coupling with the incident H-field. The current distribution at the bottom is shown in Figure 7b, which shows that current distributions are parallel, inducing the electric resonance. Figure 7c shows the current distribution for the second resonance mode. Antiparallel currents are observed along with parallel current flows. In Figure 6d, circular antiparallel current flows indicate a strong magnetic response.

In addition to the surface current distributions, electric and magnetic field distributions are given in Figure 8 to explain the resonance mechanism. The electric field distribution at 0.49 THz is shown in Figure 8a. The field is concentrated in the small square patches. The electric field distribution at 0.69 THz shown in Figure 8b is strong at the edge of the unit cell. The magnetic field distribution at 0.49 THz, shown in Figure 8c, is strongly concentrated at the center patch and those directly connected. Finally, the magnetic field distribution at

https://doi.org/10.1021/acsomega.2c06118
ACS Omega 2022, 7, 38094−38104

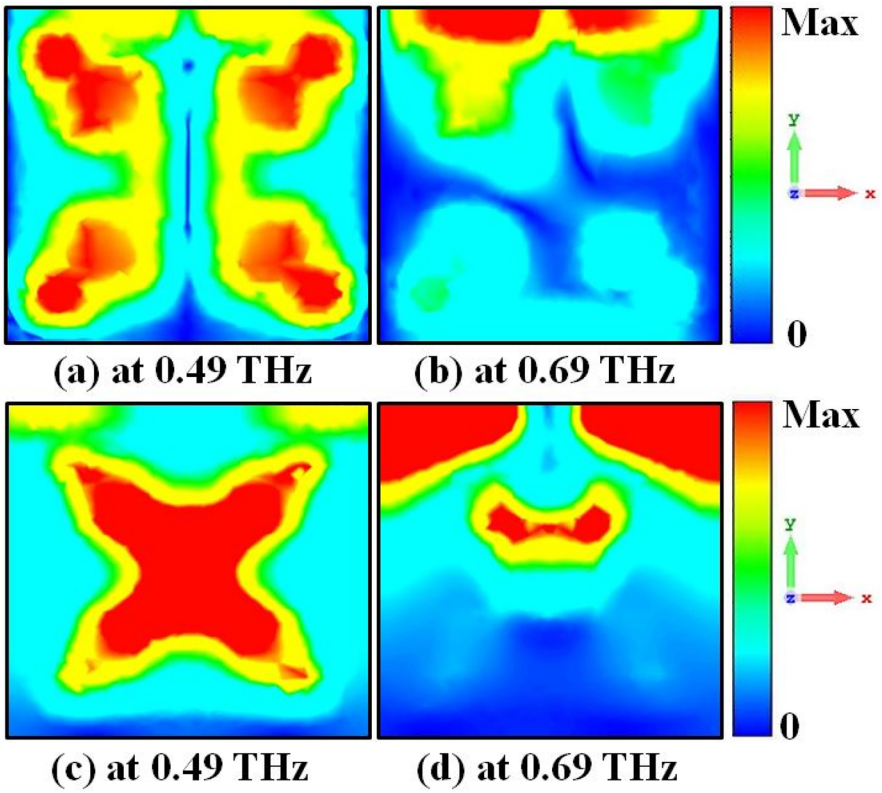

Figure 8. Color map of the field distributions of proposed metamaterial structure: (a) electric field at 0.49 THz, (b) electric field at 0.69 THz, (c) magnetic field at 0.49 THz, and (d) magnetic field 0.69 THz.

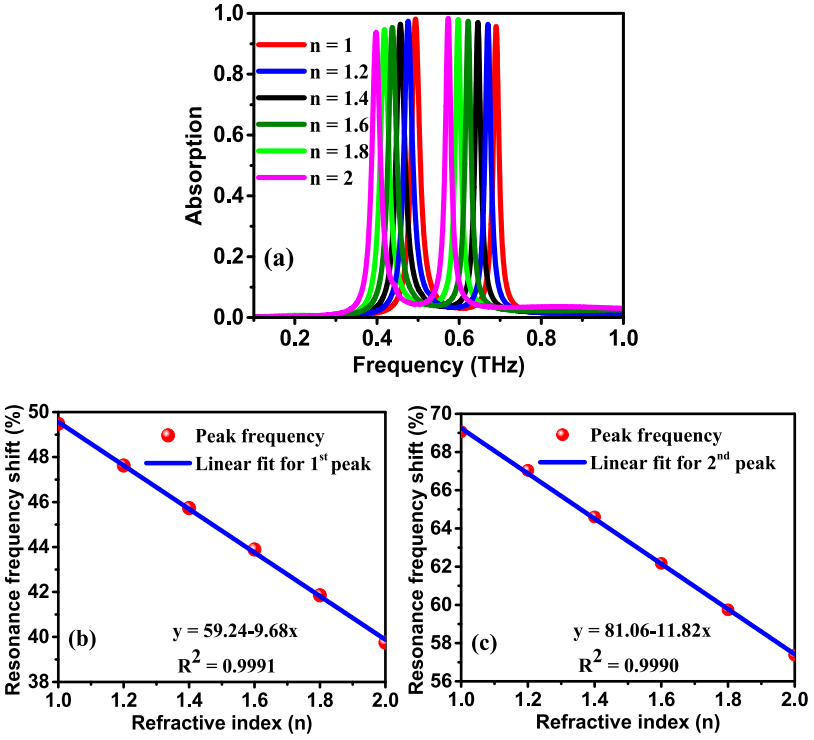

Figure 9. (a) Absorption spectrum dependence on the variation of refractive index for the surrounding environment and (b,c) resonance frequency peak with the linear fit of the two frequencies versus the refractive index.

0.69 THz in Figure 8d shows a strong concentration along the diagonal at the top edge of the unit cell. The distribution nature of the electric and magnetic fields in the aforementioned plots is attributed to the current flow distributions whether they are in a parallel flow or in an antiparallel flow. The parallel flow can induce an internal magnetic field which opposes the externally exposed one (H-field) and vice versa. The graphics in Figure 7 and Figure 8 were obtained via the

https://doi.org/10.1021/acsomega.2c06118
ACS Omega 2022, 7, 38094−38104

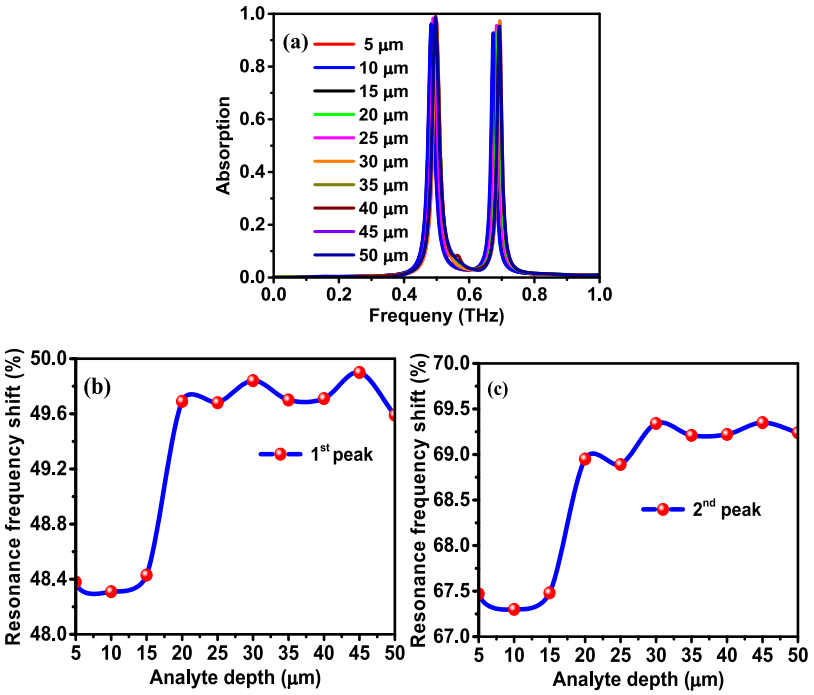

Figure 10. (a) Absorption spectrum dependence on the variation of the analyte depth and (b,c) frequency shift versus different analyte depth.

CST microwave studio program, in which the values were normalized in the settings panel. For a better view angle and understanding of the plots, the setting values were changed accordingly.

4. SENSING PERFORMANCE

The effect of the index of refraction on the absorption was also investigated. We considered the thickness of the analyte layer to be 10 μm in the numerical software, as shown in Figure 9. The resonance frequency value was shifted to the left when the refractive index was increased. Only a small change was observed in the absorption values of the proposed structure. For the first peak, the absorption was reduced with the increase in the refractive index. The reverse phenomenon was observed for the second peak. Thus, the design can help in sensing the refractive index of the surrounding environment. The sensitivity of the absorber was calculated numerically from the linear fit shown in Figure 9b,c. The resonance frequency was plotted as a function of the refractive index, and the sensitivities were measured from the linear fit of Figure 9b,c. The sensitivity was found to be 0.0968 THz/RIU for the first peak and 0.1182 THz/RIU for the second peak. In addition, it has been observed that the R^2 values are close to unity, indicating that refractive index change has a significant impact on resonance frequency shifts.

Figure 10 shows the effect of analyte depth on the absorption characteristics and frequency shift in the first and second resonance peaks. One can see that the absorption was above 90% in all of the cases. A major change in the resonance frequency occurred when the thickness was increased from 15 to 20 μm. In Figure 10b,c, the resonance frequencies for different analyte thicknesses were examined separately for the first and second peaks. Alteration in the resonance frequency for both peaks occurred at similar rates. The spectral shift (SF) of the reflection resonance dip was employed as an assessment index to evaluate the sensing performance of the MTMA, which is calculated by SF = $(f - f_0)/f_0 \times 100\%$. Here, f and f_0 are central frequencies of the reflection dip with and without the analyte, respectively. The value of SF for the first peak and second peak was found to be 2.08 and 2.98, respectively. The presence of ripples in the curves of the frequency shift with the change of analyte thickness can be attributed to the nonuniform distribution of the electromagnetic energy within the analyte.

5. EXPERIMENTAL PROTOTYPE AND RESULTS

As shown in Figure 11, the proposed design was manufactured using a 10 μm thick "PET" layer with a 2 μm coated aluminum film. Ethanol and acetone were first used to clean a 3 mm quartz wafer. Tweezers were then used to delicately lay the cleaned PET−aluminum film onto the wafer's surface. Because acetone volatilizes quickly, pressing the two layers fast and accurately was required to minimize air between the substance

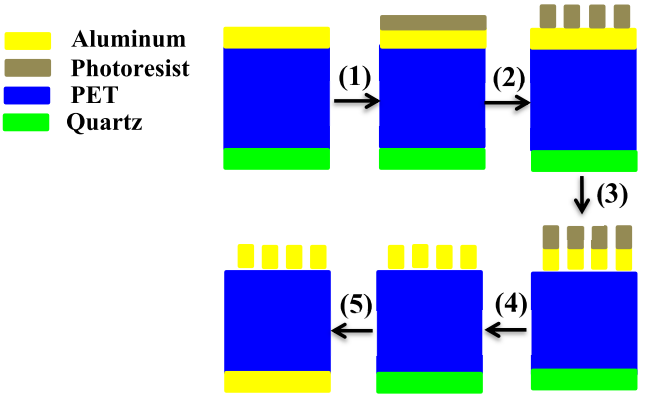

Figure 11. Process flow: (1,2) photolithography to define the metamaterial geometry, (3,4) wet etching and washing of the photoresist to fabricate the metamaterial structures, and (5) evaporation of metallic substrate layer on another side of "PET" layer.

https://doi.org/10.1021/acsomega.2c06118
ACS Omega 2022, 7, 38094−38104

and the wafer surface. The substance appeared to be adsorbed to the wafer due to the comparatively flat surface. The sample was then spin-coated with positive liquid photoresist RZJ-304 and baked for 90 s at 100 °C. Finally, the sample was moved to the photolithography processing machine, where a 60 × 60 mm^2 array was fabricated. The part of the altered photoresist was washed with a developer for 30 s after processing. The exposed metal was then etched with aluminum. The metamaterial structures were obtained as a result of this. Finally, acetone was used to clean the sample and remove the remaining photoresist. Consequently, a 2 μm thick metallic aluminum layer was produced on the other side of the PET layer using a vacuum evaporation process. A metamaterial of 60 × 60 mm^2 periodic metallic arrays with a dimension of 9 × 9 mm^2 was produced, as illustrated in Figure 12, using an

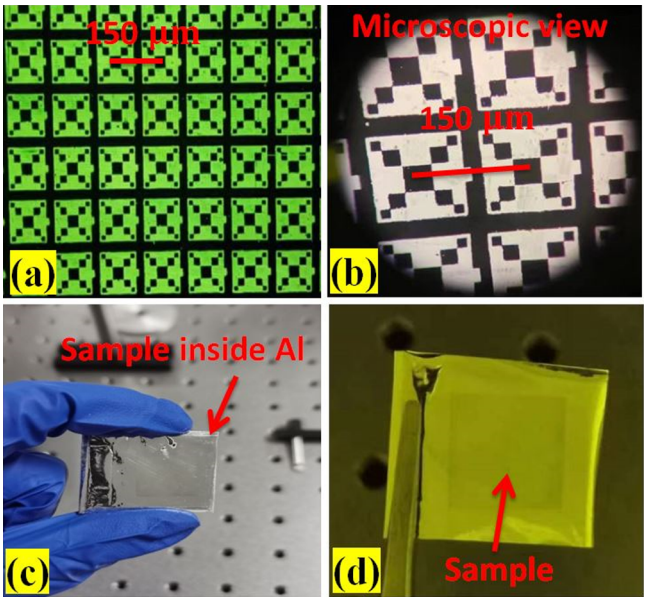

Figure 12. (a) Microscopic image of the fabricated design, (b) zoomed-in image of the proposed structure, (c) fabricated MTM absorber inside the Al thin film, and (d) view of the sample under yellow lamp light inside Al.

optical microscopy photograph of a section of the fabricated absorber structure. Terahertz time-domain spectroscopy was used to characterize the reflection spectra. The periodic boundary condition was addressed while the sample was irradiated by a light source with a spot diameter of 6 mm.

Figure 13 shows the simulated results and the experimental results for the reflection coefficient and absorption spectrum. Figure 12a presents the reflection spectrum for the proposed structure compared with the experimental results. As can be seen from the graph, the reflection spectra have two intense peaks at 0.51 and 0.7 GHz. Figure 12b shows the absorption spectrum for both numerical results and experimental results, in which there are two peaks at 0.49 and 0.69 THz corresponding to more than 90% absorptivity. No obvious noises were noticed except some deviations from the simulated results. This can be due to the reproducibility of the experimental setup, which is in good agreement with the numerical results, validating the design and its sensing performance.

The Q-factor was recalculated by using this equation:[43]

$$Q\text{-factor} = \frac{f_r}{\Delta f} \tag{2}$$

where the resonance frequency f_r is the frequency at which the real part of the impedance reaches its maximum and Δf is the width of the peak at its half-height. The Q values for the first and second peaks were calculated to be 70 and 126, respectively.

Table 1 shows the results of the proposed structure compared with those from other published metamaterial absorbers in the terahertz range in terms of techniques used, shape of the unit cell, operating frequency range, substrate materials, absorptivity, and fabricated structure. It can be seen from the table that our metamaterial design (fabricated and tested using lithography techniques) is very useful for the THz devices. The results showed that the proposed structure outperformed those reported in the literature.

Table 2 shows the comparison of the proposed metamaterials absorber with similar works in terms of the number of absorption band, the value of Q-factor, and sensitivity.

6. CONCLUSIONS

In this paper, a novel THz MTMA has been designed and demonstrated experimentally, which consists of Pythagorean tree fractals. The design offers two distinct absorption peaks at 0.49 and 0.69 THz. Investigation of the absorption mechanism revealed that the design behaves as an ENM at the first resonance frequency and as an MNM at the second frequency. Thus, the structure is unique, and resonances are plasmonic and magnetic in nature. Parametric analysis has been carried out to justify the design parameters. The resonance peaks shifted with the variation in the refractive index of the

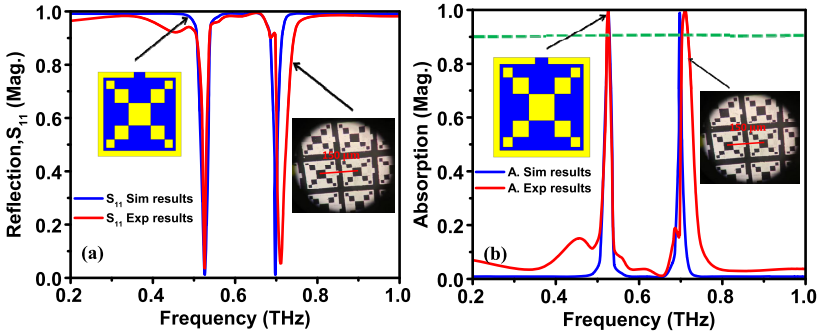

Figure 13. (a) Simulated and experimental results showed the reflection coefficient and (b) absorption spectrum for the proposed MTM absorber simulated and test results.

https://doi.org/10.1021/acsomega.2c06118
ACS Omega 2022, 7, 38094−38104

Table 1. Comparison between Our Design and Existing Metamaterials in Terms of Various Features

ref	techniques used	shape of the MTM unit cell	frequency operating THz	material substrate	absorptivity	experiment (practical)
23	bulk Dirac semimetal/photonic crystal/Au	Dirac semimetal	1−3	photonic crystal plate	0.97, 0.98, 0.99	no
24	graphene/Topas//Au	three square graphene	0.5−4.5	Topas spacer	0.99, 0.98, 0.99	no
33	Au/dielectric Teflon/Au	array of defected metallic patches (SRR)	1−2.2	dielectric Teflon	0.99	no
35	Au/dielectric layer/Au	two identical square metallic patches	1−3	dielectric layer	0.99, 0.99	no
37	graphene/Au/SiO_2/Au	folded split-ring graphene	2−6	SiO_2	0.99	no
current work	Al/PET/Al	Pythagorean tree fractal	0−1	PET	0.99, 0.97	yes

Table 2. Comparison between This Study and Other Published Work in Terms of Number of Absorption Band, Value of *Q*-Factor, and Sensitivity

ref	number of bands	Q value	sensitivity GHz/RIU
23	4	131.9, 86.9, 93.4, 45.6	
25	broad band		
33	1	22.05	300
35	2	296.27	1901
37	1	13.76	851
this work	2	70, 126	96.8, 118.2

surrounding medium and with the analyte thickness. For the refractive index, the first peak offered a sensitivity of 0.0968 THz/RIU, and the second peak offered a sensitivity of 0.1182 THz/RIU. The spectral shift of the reflection resonance dip denoted was evaluated as an assessment index to evaluate the sensing performance of the new structure, and it was found to be 2.08 and 2.98, respectively. The design can be used as a hybrid sensor for measuring the refractive index and analyte thickness in applications of biomedical sensing. In future works, the proposed design can be further investigated to show the dynamic tunability of optical responses and sensing performance in comparison to those reported in the literature.[44,45]

AUTHOR INFORMATION

Corresponding Author

Jian Dong − *School of Computer Science and Engineering, Central South University, Changsha 410075, China*; Email: dongjian@csu.edu.cn

Authors

Yadgar I. Abdulkarim − *School of Computer Science and Engineering, Central South University, Changsha 410075, China; Medical Physics Department, College of Medicals & Applied Science, Charmo University, 46023 Sulaimania, Iraq*; orcid.org/0000-0002-2808-2867

Olcay Altintas − *Department of Electrical-Electronics Engineering, Iskenderun Technical University, 31200 Hatay, Turkey*

Ayoub Sabir Karim − *Physics Department, College of Education, Salahaddin University-Erbil, 44002 Erbil, Iraq*

Halgurd N. Awl − *Department of Communication Engineering, Sulaimani Polytechnic University, 46001 Sulaimani, Iraq*

Fahmi F. Muhammadsharif − *Department of Physics, Faculty of Science and Health, Koya University, 44023 Koya, Iraq*

Fatih Özkan Alkurt − *Department of Electrical-Electronics Engineering, Iskenderun Technical University, 31200 Hatay, Turkey*

Mehmet Bakir − *Department of Computer Engineering, Bozok University, 66200 Yozgat, Turkey*

Bhargav Appasani − *School of Electronics Engineering, KIIT University, 751024 Bhubaneswar, India*

Muharrem Karaaslan − *Department of Electrical-Electronics Engineering, Iskenderun Technical University, 31200 Hatay, Turkey*

Complete contact information is available at: https://pubs.acs.org/10.1021/acsomega.2c06118

Funding

This research was funded in part by the National Natural Science Foundation of China, Grant Nos. 61801521 and 61971450, in part by the Natural Science Foundation of Hunan Province, Grant Nos. 2018JJ2533 and 2022JJ30052, and in part by the Fundamental Research Funds for the Central Universities, Grant Nos. 2018gczd014 and 20190038020050.

Notes

The authors declare no competing financial interest.

REFERENCES

(1) Fan, S. W.; Zhao, S. D.; Cao, L.; Zhu, Y.; Chen, A. L.; Wang, Y. F.; Donda, K.; Wang, Y. S.; Assouar, B. Reconfigurable curved metasurface for acoustic cloaking and illusion. *Phys. Rev. B* **2020**, *101* (2), No. 024104.

(2) Ramaccia, D.; Sounas, D. L.; Alù, A.; Bilotti, F.; Toscano, A. Nonreciprocity in antenna radiation induced by space-time varying metamaterial cloaks. *IEEE Antennas Wirel. Propag. Lett.* **2018**, *17* (11), 1968−1972.

(3) Zhang, Y.; He, Y.; Wang, H.; Sun, L.; Su, Y. Ultra-broadband mode size converter using on-chip metamaterial-based Luneburg lens. *ACS Photonics* **2021**, *8* (1), 202−208.

(4) Xu, R.; Chen, Z. N. A Transformation-Optics-Based Flat Metamaterial Luneburg Lens Antenna with Zero Focal Length. *IEEE Trans. Antennas Propag.* **2022**, *70* (5), 3287−3296.

(5) Ali, H. O.; Al-Hindawi, A. M.; Abdulkarim, Y. I.; Nugoolcharoenlap, E.; Tippo, T.; Alkurt, F. O.; Altintas, O.; Karaaslan, M. Simulated and experimental studies of multi-band symmetric metamaterial absorber with polarization independent for radar applications. *Chinese Physics B* **2022**, *31* (5), No. 058401.

(6) Xu, H.; Zhang, G.; Wang, Y.; Ning, M.; Ouyang, B.; Zhao, Y.; Huang, Y.; Liu, P. Size-Dependent Oxidation-Induced Phase Engineering for MOFs Derivatives Via Spatial Confnement Strategy Toward Enhanced Microwave Absorption. *Nano-Micro Lett.* **2022**, *14*, 102.

(7) Liu, P.; Wang, Y.; Zhang, G.; Huang, Y.; Zhang, R.; Liu, X.; Zhang, X.; Che, R. Hierarchical Engineering of Double-Shelled Nanotubes toward Hetero-Interfaces Induced Polarization and Microscale Magnetic Interaction. *Adv. Funct. Mater.* **2022**, *32* (33), 2202588.
(8) Liu, P.; Gao, S.; Zhang, G.; Huang, Y.; You, W.; Che, R. Hollow Engineering to Co@N-Doped Carbon Nanocages via Synergistic Protecting-Etching Strategy for Ultrahigh Microwave Absorption. *Adv. Funct. Mater.* **2021**, *31*, 2102812.
(9) Sağık, M.; Altıntaş, O.; Ünal, E.; Özdemir, E.; Demirci, M.; ÇOlak, Ş.; Karaaslan, M. Optimizing the gain and directivity of a microstrip antenna with metamaterial structures by using artificial neural network approach. *Wirel. Pers. Commun.* **2021**, *118* (1), 109−124.
(10) Zhang, K.; Soh, P. J.; Yan, S. Meta-wearable antennas—a review of metamaterial based antennas in wireless body area networks. *Materials* **2021**, *14* (1), 149.
(11) Öztürk, M.; Sevim, U. K.; Altıntaş, O.; Ünal, E.; Akgöl, O.; Karaaslan, M.; Sabah, C. Design of a linear to circular polarization converter integrated into a concrete construction for radome applications. *Int. J. Microw. Wirel. Technol.* **2022**, *14* (7), 824−831.
(12) Cheng, Y.; Wang, J. Tunable terahertz circular polarization convertor based on graphene metamaterial. *Diamond Relat. Mater.* **2021**, *119*, 108559.
(13) Altıntaş, O.; Aksoy, M.; Ünal, E. Design of a metamaterial inspired omega shaped resonator based sensor for industrial implementations. *Phys. E (Amsterdam, Neth.)* **2020**, *116*, 113734.
(14) Tamer, A.; Karadağ, F.; Ünal, E.; Abdulkarim, Y. I.; Deng, L.; Altintas, O.; Bakır, M.; Karaaslan, M. Metamaterial based sensor integrating transmission line for detection of branded and unbranded diesel fuel. *Chem. Phys. Lett.* **2020**, *742*, 137169.
(15) Wang, Y.; Sun, Z.; Xu, D.; Wu, L.; Chang, J.; Tang, L.; Jiang, Z.; Jiang, B.; Wang, G.; Chen, T.; Feng, H.; Yao, J. A hybrid method based region of interest segmentation for continuous wave terahertz imaging. *J. Phys. D: Appl. Phys.* **2020**, *53* (9), No. 095403.
(16) Liebermeister, L.; Nellen, S.; Kohlhaas, R. B.; Lauck, S.; Deumer, M.; Breuer, S.; Schell, M.; Globisch, B. Optoelectronic frequency-modulated continuous-wave terahertz spectroscopy with 4 THz bandwidth. *Nat. Commun.* **2021**, *12*, 1071.
(17) Chen, L.; Liao, D. G.; Guo, X. G.; Zhao, J. Y.; Zhu, Y. M.; Zhuang, S. L. Terahertz time-domain spectroscopy and micro-cavity components for probing samples: a review. *Front. Inf. Technol. Electron. Eng.* **2019**, *20* (5), 591−607.
(18) Agulto, V. C.; Toya, K.; Phan, T. N. K.; Mag-usara, V. K.; Li, J.; Empizo, M. J. F.; Iwamoto, T.; Goto, K.; Murakami, H.; Kumagai, Y.; Sarukura, N.; Yoshimura, M.; Nakajima, M. Anisotropic complex refractive index of β-Ga2O3 bulk and epilayer evaluated by terahertz time-domain spectroscopy. *Appl. Phys. Lett.* **2021**, *118* (4), No. 042101.
(19) Borovkova, M.; Khodzitsky, M.; Demchenko, P.; Cherkasova, O.; Popov, A.; Meglinski, I. Terahertz time-domain spectroscopy for non-invasive assessment of water content in biological samples. *Biomed. Opt. Express* **2018**, *9* (5), 2266−2276.
(20) Hillger, P.; Jain, R.; Grzyb, J.; Förster, W.; Heinemann, B.; MacGrogan, G.; Mounaix, P.; Zimmer, T.; Pfeiffer, U. R. A 128-pixel system-on-a-chip for real-time super-resolution terahertz near-field imaging. *IEEE J. Solid-State Circuits* **2018**, *53* (12), 3599−3612.
(21) Pogna, E. A.; Asgari, M.; Zannier, V.; Sorba, L.; Viti, L.; Vitiello, M. S. Unveiling the detection dynamics of semiconductor nanowire photodetectors by terahertz near-field nanoscopy. *Light: Sci. Appl.* **2020**, *9*, 189.
(22) Cheng, X.; Huang, R.; Xu, J.; Xu, X. Broadband terahertz near-perfect absorbers. *ACS Appl. Mater. Interfaces* **2020**, *12* (29), 33352−33360.
(23) Wang, Y.; Yi, Y.; Xu, D.; Yi, Z.; Li, Z.; Chen, X.; Jile, H.; Zhang, J.; Zeng, L.; Li, G. Terahertz tunable three band narrowband perfect absorber based on Dirac semimetal. *Phys. E (Amsterdam, Neth.)* **2021**, *131*, 114750.
(24) Liu, L.; Liu, W.; Song, Z. Ultra-broadband terahertz absorber based on a multilayer graphene metamaterial. *J. Appl. Phys.* **2020**, *128* (9), No. 093104.
(25) Son, J. H.; Oh, S. J.; Cheon, H. Potential clinical applications of terahertz radiation. *J. Appl. Phys.* **2019**, *125* (19), 190901.
(26) Nikitkina, A. I.; Bikmulina, P. Y.; Gafarova, E. R.; Kosheleva, N. V.; Efremov, Y. M.; Bezrukov, E. A.; Butnaru, D. V.; Dolganova, I. N.; Chernomyrdin, N. V.; Cherkasova, O. P.; Gavdush, A. A.; Timashev, P. S. Terahertz radiation and the skin: a review. *J. Biomed. Opt.* **2021**, *26* (4), No. 043005.
(27) Zhang, L. L.; Wang, W. M.; Wu, T.; Feng, S. J.; Kang, K.; Zhang, C. L.; Zhang, Y.; Li, Y. T.; Sheng, Z. M.; Zhang, X. C. Strong terahertz radiation from a liquid-water line. *Phys. Rev. Appl.* **2019**, *12* (1), No. 014005.
(28) Holloway, J. W.; Dogiamis, G. C.; Han, R. Innovations in terahertz interconnects: High-speed data transport over fully electrical terahertz waveguide links. *IEEE Microw. Mag.* **2020**, *21* (1), 35−50.
(29) Paul, B. K.; Ahmed, K. Analysis of terahertz waveguide properties of Q-PCF based on FEM scheme. *Opt. Mater.* **2020**, *100*, 109634.
(30) Headland, D.; Withayachumnankul, W.; Yu, X.; Fujita, M.; Nagatsuma, T. Unclad microphotonics for terahertz waveguides and systems. *J. Lightwave Technol.* **2020**, *38* (24), 6853−6862.
(31) Ye, J.; Dang, S.; Ma, G.; Amin, O.; Shihada, B.; Alouini, M. S. On outage performance of terahertz wireless communication systems. *IEEE Trans. Commun.* **2022**, *70* (1), 649−663.
(32) Abohmra, A.; Khan, Z. U.; Abbas, H. T.; Shoaib, N.; Imran, M. A.; Abbasi, Q. H. Two-dimensional Materials for Future Terahertz Wireless Communications. *IEEE Open J. Antennas Propag.* **2022**, *3*, 217−228.
(33) Saadeldin, A. S.; Hameed, M. F. O.; Elkaramany, E. M.; Obayya, S. S. Highly sensitive terahertz metamaterial sensor. *IEEE Sens. J.* **2019**, *19* (18), 7993−7999.
(34) Yang, J.; Lin, Y. S. Design of tunable terahertz metamaterial sensor with single-and dual-resonance characteristic. *Nanomaterials* **2021**, *11* (9), 2212.
(35) Wang, B. X.; He, Y.; Lou, P.; Xing, W. Design of a dual-band terahertz metamaterial absorber using two identical square patches for sensing application. *Nanoscale Adv.* **2020**, *2* (2), 763−769.
(36) Keshavarz, A.; Vafapour, Z. Sensing avian influenza viruses using terahertz metamaterial reflector. *IEEE Sens. J.* **2019**, *19* (13), 5161−5166.
(37) Nickpay, M. R.; Danaie, M.; Shahzadi, A. Highly sensitive THz refractive index sensor based on folded split-ring metamaterial graphene resonators. *Plasmonics* **2022**, *17* (1), 237−248.
(38) Yang, J.; Qi, L.; Li, B.; Wu, L.; Shi, D.; Ahmed Uqaili, J.; Tao, X. A terahertz metamaterial sensor used for distinguishing glucose concentration. *Results Phys.* **2021**, *26*, 104332.
(39) Askari, M.; Pakarzadeh, H.; Shokrgozar, F. High Q-factor terahertz metamaterial for superior refractive index sensing. *JOSA B* **2021**, *38* (12), 3929−3936.
(40) Wang, G.; Zhu, F.; Lang, T.; Liu, J.; Hong, Z.; Qin, J. All-metal terahertz metamaterial biosensor for protein detection. *Nanoscale Res. Lett.* **2021**, *16*, 109.
(41) Smith, D. R.; Padilla, W. J.; Vier, D. C.; Nemat-Nasser, S. C.; Schultz, S. Composite Medium with Simultaneously Negative Permeability and Permittivity. *Phys. Rev. Lett.* **2000**, *84* (18), 4184−4187.
(42) Yuan, H. K.; Chettiar, U. K.; Cai, W.; Kildishev, A. V.; Boltasseva, A.; Drachev, V. P.; Shalaev, V. M. A negative permeability material at red light. *Opt. Express* **2007**, *15* (3), 1076−1083.
(43) Abdulkarim, U. I.; Xiao, M.; Awl, H. N.; Muhammadsharif, F. F.; Lang, T.; Saeed, S. R.; Alkurt, F. Ö.; Bakır, M.; Karaaslan, M.; Dong, J. Simulation and lithographic fabrication of a triple band terahertz metamaterial absorber coated on flexible polyethylene terephthalate substrate. *Opt. Mater. Express* **2022**, *12* (1), 338−359.
(44) Xiao, S.; Wang, T.; Liu, T.; Zhou, C.; Jiang, X.; Zhang, J. Active metamaterials and metadevices: a review. *J. Phys. D: Appl. Phys.* **2020**, *53*, 503002.

https://doi.org/10.1021/acsomega.2c06118
ACS Omega 2022, 7, 38094−38104

(45) Guanxing, Z.; Liu, Z.; Deng, W.; Zhu, W. Reconfigurable metasurfaces with mechanical actuations: towards flexible and tunable photonic devices. *J. Opt.* **2021**, *23*, No. 013001.

https://doi.org/10.1021/acsomega.2c06118
ACS Omega 2022, 7, 38094−38104